

Orbital magnetic moments in SrRuO₃ epitaxial thin films with interfacially controlled magnetic anisotropy

Daisuke Kan,¹ Masaichiro Mizumaki,² Tomoe Nishimura,¹ and Yuichi Shimakawa^{1,3}

¹*Institute for Chemical Research, Kyoto University, Uji, Kyoto 611-0011, Japan*

²*Japan Synchrotron Radiation Research Institute, SPring-8, Sayo, Hyogo 679-5198, Japan*

³*Integrated Research Consortium on Chemical Sciences, Uji, Kyoto 611-0011, Japan*

(Received 29 August 2016; revised manuscript received 15 November 2016; published 19 December 2016)

Using x-ray absorption spectroscopy (XAS) and x-ray magnetic circular dichroism (XMCD) spectroscopy, we evaluated the orbital magnetic moments of itinerant ferromagnet SrRuO₃ (SRO) epitaxial thin films with interfacially controlled magnetic anisotropy. We found that the orbital moment is closely correlated with the SRO's magnetic anisotropy, which can be controlled by interfacially engineering the RuO₆ octahedral rotations. For the monoclinic film with magnetization along the direction 45° from the out-of-plane direction, the orbital moment is $\approx -0.1 \mu_B/\text{Ru}$ along the magnetic easy axis direction and is aligned antiparallel to the direction of the spin magnetic moments. For the tetragonal film with in-plane magnetization, on the other hand, the out-of-plane component of the orbital moment is as small as $\approx -0.04 \mu_B/\text{Ru}$, accounting for the film's in-plane magnetic anisotropy. Our results highlight that the magnetic anisotropy of SRO can be controlled by engineering the orbital magnetic moment through the octahedral distortions.

DOI: [10.1103/PhysRevB.94.214420](https://doi.org/10.1103/PhysRevB.94.214420)

I. INTRODUCTION

An orbital magnetic moment plays a key role in determining magnetic anisotropy through spin-orbit interactions in ferromagnets. It has been shown [1–6] that the orbital moment along a perpendicular direction is induced in artificial superstructures such as multilayers and heterostructures and that it is often attributed to either interfacial electronic hybridizations or structural distortions accommodated in the superstructures. In fact, such an induced orbital moment stabilizes perpendicular magnetic anisotropy in ultrathin magnetic layers [7,8], which are expected to be used in next-generation nonvolatile high-density memory devices. It is therefore important to evaluate the orbital magnetic moment in artificial superstructures and to see how it affects their magnetic anisotropy.

It has been shown [9–16] that magnetic anisotropy in thin films of ferromagnetic transition metal oxides is often modified by lattice-mismatch-induced epitaxial strains, film thicknesses, and interfacial structures that affect oxygen coordination environments surrounding the transition metals or distort the oxygen octahedra in oxides. An important implication for the modified magnetic anisotropy in the films is that the orbital magnetic moment strongly depends on the oxygen environments. Recent investigations have demonstrated [9,10,17,18] that interfacial engineering of the oxygen environments (or oxygen octahedral distortions) is a promising approach to controlling the film's magnetic anisotropy, without changing either its chemical composition or thickness and thereby causing additional side effects. This interfacial engineering thus provides opportunities for investigating how the orbital moment is affected by the oxygen environments or oxygen octahedral distortions in oxide films.

In this study, we used x-ray absorption spectroscopy (XAS) and x-ray magnetic circular dichroism (XMCD) spectroscopy and quantitatively evaluated the orbital magnetic moments of SrRuO₃ (SRO) films with interfacially engineered uniaxial magnetic anisotropy. Previous investigations have shown that the magnetic anisotropy of (110)_{ortho} SRO films epitaxi-

ally grown on (110)_{ortho} GdScO₃ (GSO) substrates can be engineered by inserting unit-cell-thick Ca_{0.5}Sr_{0.5}TiO₃ (CSTO) layers at the film/substrate interface [9,15,17] (where the subscript ortho denotes the orthorhombic perovskite notation). Our XAS and XMCD characterizations show that the orbital moments in the SRO films are anisotropic depending on the interfacial CSTO layer thickness. This indicates that orbital magnetic moments play an important role in determining the magnetic anisotropy of the films.

II. EXPERIMENTAL DETAILS

The SRO/CSTO/GSO heterostructures were made by pulsed laser deposition. The CSTO buffer layer was grown on the (110)_{ortho} GSO substrate at 700 °C under an oxygen partial pressure of 1×10^{-5} Torr. The thickness of the CSTO buffer layer, which determines the SRO's structural phase [9], was controlled in a layer-by-layer manner by *in-situ* monitoring of the oscillations of reflection high-energy electron diffraction (RHEED) spot intensity. After the buffer layer was deposited, the 10-nm-thick SRO layer was deposited at the same temperature under an oxygen partial pressure of 100 m Torr. The monoclinic and tetragonal SRO layers with distinct magnetic anisotropy (referred to as m-SRO and t-SRO, respectively) were grown on the substrates buffered with two- and three-monolayer-thick CSTO layers, respectively. We note that all prepared SRO films exhibited metallic conduction down to low temperatures and underwent the ferromagnetic transition at around 120–130 K.

III. RESULTS AND DISCUSSION

Figures 1(a) and 1(b) show x-ray reciprocal space mappings for SRO/CSTO/GSO heterostructures with the CSTO layers two and three monolayers thick. The mappings were obtained around the (620)_{ortho}, (260)_{ortho}, and (444)_{ortho} GSO reflections. It is obvious that for both heterostructures, all observed reflections from the SRO layer appear in the same position

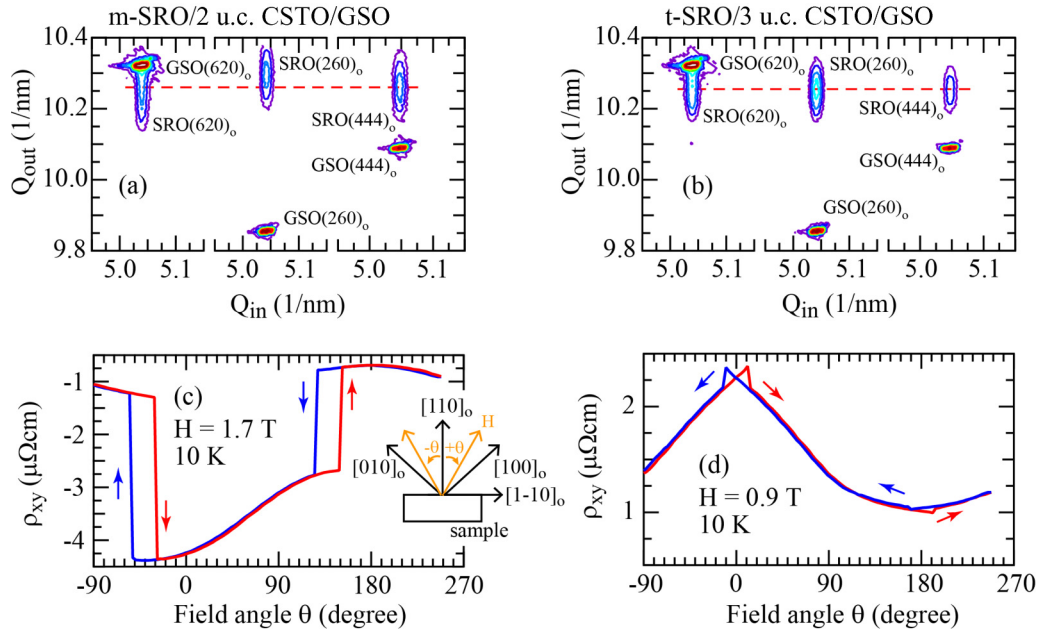


FIG. 1. X-ray diffraction and magnetotransport characterizations for (a, c) m-SRO/2 u.c. CSTO/GSO and (b, d) t-SRO/3 u.c. CSTO/GSO heterostructures. X-ray reciprocal space mappings in (a) and (b) were taken around the $(620)_{\text{ortho}}$, $(260)_{\text{ortho}}$, and $(444)_{\text{ortho}}$ GSO reflections. Magnetic field angle dependence of the transverse Hall resistivity in (c) and (d) was evaluated at 10 K and by rotating a magnetic field of either 1.7 Tesla (for the m-SRO film) or 0.9 Tesla (for the t-SRO film) in clockwise and counterclockwise directions within the $(001)_{\text{ortho}}$ plane of the GSO substrate. The inset in (c) shows the definition of the magnetic field angle θ . Note that the $[110]_0$ direction corresponds to the growth direction of the SRO films

along the horizontal axis (the in-plane direction) as those of the reflections from the substrate, confirming that the entire heterostructure was coherently grown. Importantly, the vertical positions of the $(620)_{\text{ortho}}$, $(260)_{\text{ortho}}$, and $(444)_{\text{ortho}}$ SRO reflections for the heterostructure with the two-monolayer-thick CSTO layer are all different [Fig. 1(a)]. The SRO reflections for the heterostructure with the three-monolayer-thick CSTO layer, on the other hand, all appear in the same position along the vertical axis [Fig. 1(b)]. These observations confirm that two- and three-monolayer-thick CSTO layers stabilize the monoclinic and tetragonal structural phases of the SRO layer, respectively. Our synchrotron x-ray diffraction study [19] showed that while the m- and t-SRO films are under identical substrate-induced epitaxial strain, RuO_6 octahedral rotation patterns differ between these two films. The rotation pattern of the m-SRO films is described to be $a^-b^+c^-$ in Glazer notation [20,21]. On the other hand, the t-SRO has $a^-b^0c^+$ rotation. It should be noted that both rotation angles about the $[100]_{\text{pc}}$ and $[001]_{\text{pc}}$ axes (the α_{rot} and γ_{rot} rotations) are comparable between the m- and t-SRO films and that these structural phases in SRO are distinguished by the RuO_6 rotation about the $[010]_{\text{pc}}$ axis (the β_{rot} rotation), which corresponds to the $[001]_{\text{ortho}}$ axis in the orthorhombic notation (where subscript pc denotes the pseudocubic perovskite notation). Given that the octahedral rotation is related to the Ru-O-Ru bond angle, the differences in the β_{rot} rotation are associated with the change in the bond angle on the $(010)_{\text{pc}}$ plane. In fact, annular bright field (ABF) scanning transmission electron microscopy (STEM) observations [9] revealed that the bond angle projected on the $(010)_{\text{pc}}$ plane of m-SRO is $\sim 170^\circ$, which is smaller than that of t-SRO ($\sim 180^\circ$).

Due to the strong magnetocrystalline effect of SRO, the prepared films exhibit distinct magnetic anisotropy depending on their structural phase. Figures 1(c) and 1(d) show the field angle dependence of the Hall resistivities ρ_{xy} at 10 K. Both m- and t-SRO films exhibit jumps in ρ_{xy} resulting from the magnetization reversal, which are seen every 180° , associated with the hysteresis in the clockwise and counterclockwise field rotations. We note that the center position of the hysteresis differs between m- and t-SRO films. Based on the center position of the hysteresis, it is seen that the uniaxial magnetic easy axis of m-SRO is parallel to the $[100]_{\text{ortho}}$ axis of the $\sqrt{2}a_{\text{pc}} \times \sqrt{2}a_{\text{pc}} \times 2a_{\text{pc}}$ unit cell of the m-SRO (namely, tilted by 45° with respect to the out-of-plane direction), while t-SRO has a uniaxial in-plane magnetic anisotropy with the magnetization parallel to the in-plane $[1-10]_{\text{ortho}}$ direction of the substrate. These observations are in close agreement with those made in previous studies [9,15,17].

To characterize the orbital magnetic moments of the SRO films, we measured the Ru $M_{2,3}$ -edge ($\text{Ru } 3p \rightarrow 4d$) XAS and XMCD spectra in the total electron yield mode at 20 K with circularly polarized incident beams (μ^+ and μ^-) and under a 1.9 Tesla magnetic field applied at various angles θ with respect to the surface of the heterostructures. The obtained XAS and XMCD spectra with $\theta = 0^\circ$ for m-SRO and t-SRO are presented in Fig. 2. The inset of the figure depicts the measurement configuration including the magnetic field and incident beam directions. It is noted that the incident beam is 10° off the magnetic field. The XAS spectra for each helicity of the incident beam (μ^+ and μ^-) were obtained by averaging spectra taken under a magnetic field in opposite directions. To obtain the per atomic basis XMCD spectra, the XAS spectra

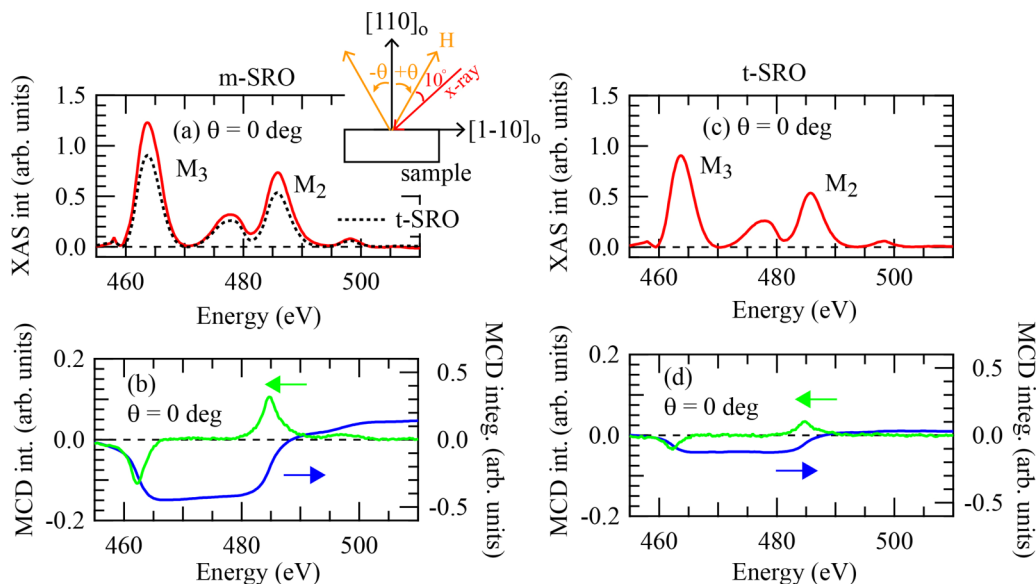


FIG. 2. Averaged Ru $M_{2,3}$ -edge XAS (red) and normalized XMCD spectra (green) for (a, b) m-SRO/CSTO/GSO and (c, d) t-SRO/CSTO/GSO heterostructures. In (a), the spectra for t-SRO (the dotted line) is also presented for comparison. The blue curves in (b) and (d) correspond to the integrated XMCD spectra. The inset in (a) shows the measurement configuration, including the applied magnetic field angle θ and the incident x-ray beam direction. For clarity, the incident beam is drawn only on the $' + \theta'$ side. The field angle is defined as shown by the inset in Fig. 1(c). The spectra in the figure were obtained under a 1.9 Tesla magnetic field normal to the sample surface (the $\theta = 0$ configuration). All data were taken at 20 K.

taken at each configuration were normalized in such a way that the edge jump in the energy region above 505 eV was unity. The measurements were made at beamline BL25SU in SPring-8.

The averaged Ru $M_{2,3}$ -edge XAS spectra $1/2(\mu^+ + \mu^-)$ with the $\theta = 0^\circ$ configuration in Figs. 2(a) and 2(c) show that regardless of the structural phase of the SRO layer (monoclinic or tetragonal), the Ru M_2 - and M_3 -edge peaks appear at 485.8 eV and 463.7 eV, respectively. These peak positions are in close agreement with the Ru $M_{2,3}$ -edge peak positions previously seen for SrRuO₃ epitaxial films [22,23]. These observations indicate that the valence state of Ru is the same in the m- and t-SRO films and that the difference between these films with regard to their oxygen coordination environment (or oxygen octahedral rotations) [9,17] has little influence on the Ru valence state. As shown in Figs. 2(b) and 2(d), clear XMCD signals ($\Delta\mu \equiv \mu^+ - \mu^-$) are seen for both m- and t-SRO films. Interestingly, the m-SRO film exhibits more pronounced signals than the t-SRO film, implying that the m-SRO has the larger out-of-plane component of magnetization.

We also found that the XMCD signals for the m-SRO film are strongly dependent on the field angle θ , and those for the t-SRO are less dependent on θ . Figure 3 shows XMCD spectra with the $\theta = +30^\circ$ and -30° configurations for the m- and t-SRO films. For m-SRO, the signal taken with the $\theta = +30^\circ$ configuration is more enhanced than the signal taken with the $\theta = -30^\circ$ configuration. For t-SRO, on the other hand, the signals taken with the $\theta = +30^\circ$ and -30° configurations are almost comparable. These observations can be understood by considering the difference in the magnetic easy axis direction between the m- and t-SRO films. As shown in Figs. 1(c)

and 1(d), the m-SRO has uniaxial magnetic anisotropy with the easy axis along the $[100]_{\text{ortho}}$ axis (corresponding to the $\theta = +45^\circ$ direction), while the t-SRO has in-plane magnetic anisotropy with the easy axis along the $[1-10]_{\text{ortho}}$ direction (or the $\theta = \pm 90^\circ$ direction).

Orbital and spin magnetic moments (m_{orb} and m_{spin}) per Ru in the m- and t-SRO films were quantitatively evaluated by applying the sum rules [24,25] to the XAS and XMCD data taken with various magnetic field directions ($-30^\circ \leq \theta \leq +60^\circ$). The m_{orb} and m_{spin} were calculated by the following equations.

$$m_{\text{orb}} = -\frac{2(10 - n_{4d})}{r} \int_{M_{2,3}} \Delta\mu dE$$

$$m_{\text{spin}} = -\frac{(10 - n_{4d})}{r} \left(\int_{M_2} \Delta\mu dE - 2 \int_{M_3} \Delta\mu dE \right)$$

where $r = \frac{1}{2} \int_{M_{2,3}} (\mu^+ + \mu^-) dE$, and n_{4d} is the number of electrons in $4d$ orbitals and is assumed to be 4. The obtained m_{orb} and m_{spin} of the m-SRO and t-SRO films are plotted against θ ($-30^\circ \leq \theta \leq +60^\circ$) in Fig. 4. The m_{orb} values calculated for configurations between $\theta = -30^\circ$ and $+60^\circ$ are all negative, although the magnitude of the m_{orb} of t-SRO is rather small. This indicates the antiparallel arrangement of m_{orb} to m_{spin} in the SRO films. A key observation is that the m_{orb} of m-SRO is strongly dependent on θ , namely anisotropic, exhibiting a minimum of $\approx -0.1 \mu_B/\text{Ru}$ when θ is $\sim +45^\circ$, i.e., an angle at which m_{spin} shows a maximum of $1.7 \mu_B/\text{Ru}$. On the other hand, m_{orb} of the t-SRO layer is almost independent of θ and is as small as $\approx -0.04 \mu_B/\text{Ru}$. These observations indicate that the orbital magnetic moment influences the magnetic anisotropy of the

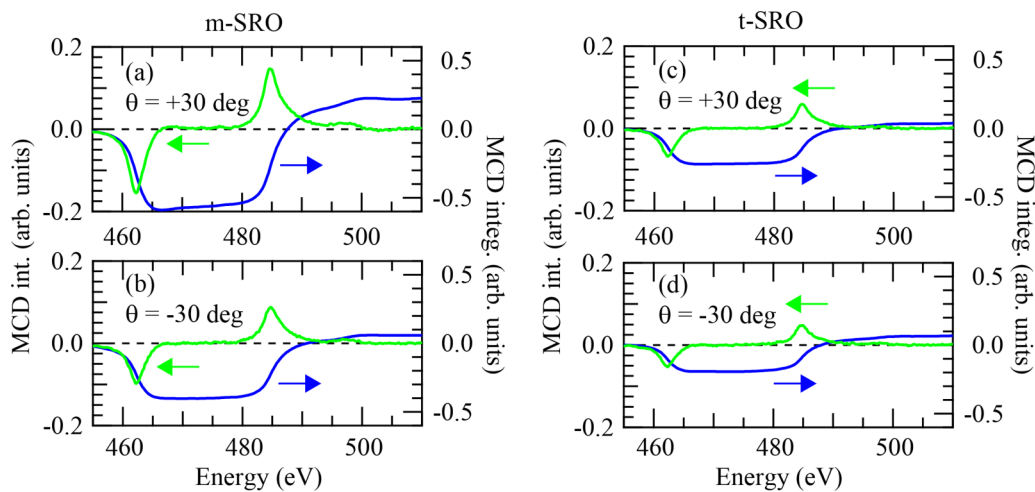


FIG. 3. Normalized Ru $M_{2,3}$ -edge XMCD spectra (green) with the with the $\theta = +30^\circ$ and -30° configurations for (a, b) m-SRO/CSTO/GSO and (c, d) t-SRO/CSTO/GSO heterostructures. The blue curves in the figures correspond to the integrated XMCD spectra. All data were taken at 20 K and under a 1.9 Tesla magnetic field.

SRO films, and they explain why the magnetic anisotropy of SRO can be controlled by interfacially engineering the RuO_6 octahedral distortions. The magnetic easy axis along the $[100]_{\text{ortho}}$ axis of the m-SRO film is stabilized by the spin-orbit coupling of m_{orb} and m_{spin} arranged antiparallel along that direction. On the other hand, the observed negligibly small perpendicular components of m_{orb} of t-SRO, which suggest an alignment of the orbital moment along the in-plane direction, are consistent with the film's in-plane magnetic anisotropy. We note that the magnetic anisotropy of the t-SRO is uniaxial, and its easy direction is parallel to the in-plane $[1-10]_{\text{ortho}}$ direction (not the in-plane $[001]_{\text{ortho}}$ direction) of the GSO substrate [9,17]. Our XMCD observations imply that the small in-plane orbital magnetic moment contributes to the uniaxial in-plane magnetic anisotropy of t-SRO, although precise evaluation of the in-plane orbital moment is difficult from our XMCD measurements. The magnetic easy axis direction of SRO is predominantly determined by the structural phase (monoclinic or tetragonal phase

with the distinct octahedral rotation) [9,15,17], indicating the significance of the octahedral rotation pattern on the behavior of the orbital magnetic moment. In particular, it is the RuO_6 octahedral rotation about the $[010]_{\text{pc}}$ direction (the β_{rot} rotation) that distinguishes between the m- and t-SRO films. Therefore, the observed differences in the anisotropy of m_{orb} between the m- and t-SRO films originate from the β_{rot} rotation, which influences electron occupations in $4d t_{2g}$ orbitals and consequently modifies both m_{orb} and m_{spin} .

It is also interesting to point out that the antiparallel arrangement of m_{orb} to m_{spin} is not seen in SrRuO_3 films epitaxially grown on other oxide substrates, such as SrTiO_3 (STO) substrates [22,26], although the magnitudes of m_{orb} are comparable among the films grown on GSO and STO substrates. Given that the RuO_6 octahedral rotation pattern in the m-SRO film on GSO ($a^-b^+c^-$ in the Glazer notation) is almost the same as that in the SRO films on STO substrates ($a^-a^+c^-$) [19,27,28], our observations imply that the

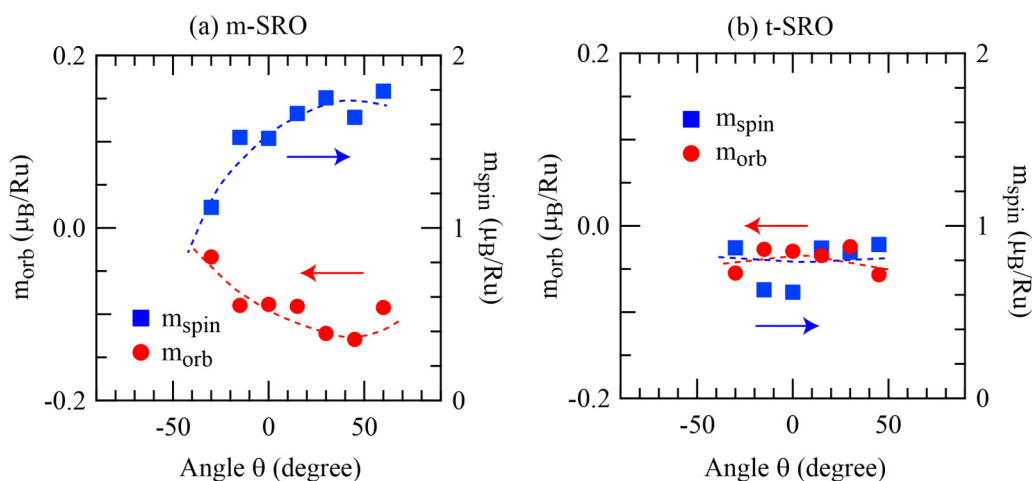


FIG. 4. The orbital and spin magnetic moments of m- and t-SRO layers as a function of applied magnetic field angle θ ($-30^\circ \leq \theta \leq +60^\circ$). The dotted lines in the figure are a guide to the eye.

substrate-induced epitaxial strain, which results in octahedral distortions, affects the directional relationships between the orbital and spin magnetic moments of SRO.

IV. SUMMARY

We performed XAS and XMCD characterizations of the orbital and spin magnetic moments in SRO epitaxial thin films with interfacially controlled magnetic anisotropy. Our results revealed that the orbital moment of the m-SRO film is $\approx -0.1 \mu_B/\text{Ru}$ along the $[100]_{\text{ortho}}$ axis and is aligned antiparallel to the $1.7 \mu_B/\text{Ru}$ spin moment, stabilizing the uniaxial magnetic easy axis of the m-SRO along that direction. On the other hand, the perpendicular component of the orbital magnetic moment of the t-SRO film is negligibly small ($\approx -0.04 \mu_B/\text{Ru}$), consistent with the film's in-plane magnetic anisotropy. These results highlight the

important role that the orbital magnetic moment plays in determining the magnetic anisotropy of SRO. This also explains why the magnetic anisotropy of SRO films can be controlled by interfacially engineering the RuO₆ octahedral distortions.

ACKNOWLEDGMENTS

This work was partially supported by a grant for the Integrated Research Consortium on Chemical Sciences and by Grants-in-Aid for Scientific Research KAKENHI (Grants No. 15K13670, No. 16H02266, and No. 16K13665) from the Ministry of Education, Culture, Sports, Science and Technology (MEXT) of Japan. The XAS and XMCD measurements at SPring-8 were made with the approval of the Japan Synchrotron Radiation Research Institute (Proposal No. 2015B1008).

-
- [1] H. A. Dürr, G. Y. Guo, G. van der Laan, J. Lee, G. Lauhoff, and J. A. C. Bland, *Science* **277**, 213 (1997).
- [2] D. Weller, Y. Wu, J. Stöhr, M. G. Samant, B. D. Hermsmeier, and C. Chappert, *Phys. Rev. B* **49**, 12888 (1994).
- [3] D. Weller, J. Stöhr, R. Nakajima, A. Carl, M. G. Samant, C. Chappert, R. Mégy, P. Beauvillain, P. Veillet, and G. A. Held, *Phys. Rev. Lett.* **75**, 3752 (1995).
- [4] N. Nakajima, T. Koide, T. Shidara, H. Miyauchi, H. Fukutani, A. Fujimori, K. Iio, T. Katayama, M. Nývlt, and Y. Suzuki, *Phys. Rev. Lett.* **81**, 5229 (1998).
- [5] J. M. Shaw, H. T. Nembach, and T. J. Silva, *Phys. Rev. B* **87**, 054416 (2013).
- [6] P. Bruno, *Phys. Rev. B* **39**, 865 (1989).
- [7] S. Ikeda, K. Miura, H. Yamamoto, K. Mizunuma, H. D. Gan, M. Endo, S. Kanai, J. Hayakawa, F. Matsukura, and H. Ohno, *Nat. Mater.* **9**, 721 (2010).
- [8] S. Mangin, D. Ravelosona, J. A. Katine, M. J. Carey, B. D. Terris, and E. E. Fullerton, *Nat. Mater.* **5**, 210 (2006).
- [9] D. Kan, R. Aso, R. Sato, M. Haruta, H. Kurata, and Y. Shimakawa, *Nat. Mater.* **15**, 432 (2016).
- [10] Z. Liao, M. Huijben, Z. Zhong, N. Gauquelin, S. Macke, R. J. Green, S. Van Aert, J. Verbeeck, G. Van Tendeloo, K. Held, G. A. Sawatzky, G. Koster, and G. Rijnders, *Nat. Mater.* **15**, 425 (2016).
- [11] H. Boschker, M. Mathews, E. P. Houwman, H. Nishikawa, A. Vailionis, G. Koster, G. Rijnders, and D. H. A. Blank, *Phys. Rev. B* **79**, 214425 (2009).
- [12] K. Terai, T. Ohnishi, M. Lippmaa, H. Koinuma, and M. Kawasaki, *Jap. J. Appl. Phys.* **43**, L227 (2004).
- [13] A. J. Grutter, F. J. Wong, C. A. Jenkins, E. Arenholz, A. Vailionis, and Y. Suzuki, *Phys. Rev. B* **88**, 214410 (2013).
- [14] A. Grutter, F. Wong, E. Arenholz, M. Liberati, A. Vailionis, and Y. Suzuki, *Appl. Phys. Lett.* **96**, 082509 (2010).
- [15] D. Kan, R. Aso, H. Kurata, and Y. Shimakawa, *Adv. Funct. Mater.* **23**, 1129 (2013).
- [16] Z. Liao, M. Huijben, G. Koster, and G. Rijnders, *APL Mater.* **2**, 096112 (2014).
- [17] R. Aso, D. Kan, Y. Shimakawa, and H. Kurata, *Adv. Funct. Mater.* **24**, 5177 (2014).
- [18] D. Kan, R. Aso, H. Kurata, and Y. Shimakawa, *J. Appl. Phys.* **115**, 184304 (2014).
- [19] D. Kan, Y. Wakabayashi, H. Tajiri, and Y. Shimakawa, *Phys. Rev. B* **94**, 024112 (2016).
- [20] A. M. Glazer, *Acta Crystallogr. B* **28**, 3384 (1972).
- [21] P. M. Woodward, *Acta Crystallogr. B* **53**, 32 (1997).
- [22] K. Ishigami, K. Yoshimatsu, D. Toyota, M. Takizawa, T. Yoshida, G. Shibata, T. Harano, Y. Takahashi, T. Kadono, V. K. Verma, V. R. Singh, Y. Takeda, T. Okane, Y. Saitoh, H. Yamagami, T. Koide, M. Oshima, H. Kumigashira, and A. Fujimori, *Phys. Rev. B* **92**, 064402 (2015).
- [23] J. Okamoto, T. Okane, Y. Saitoh, K. Terai, S. I. Fujimori, Y. Muramatsu, K. Yoshii, K. Mamiya, T. Koide, A. Fujimori, Z. Fang, Y. Takeda, and M. Takano, *Phys. Rev. B* **76**, 184441 (2007).
- [24] B. T. Thole, P. Carra, F. Sette, and G. van der Laan, *Phys. Rev. Lett.* **68**, 1943 (1992).
- [25] P. Carra, B. T. Thole, M. Altarelli, and X. Wang, *Phys. Rev. Lett.* **70**, 694 (1993).
- [26] A. J. Grutter, F. J. Wong, E. Arenholz, A. Vailionis, and Y. Suzuki, *Phys. Rev. B* **85**, 134429 (2012).
- [27] A. Vailionis, W. Siemons, and G. Koster, *Appl. Phys. Lett.* **93**, 051909 (2008).
- [28] A. Vailionis, H. Boschker, Z. Liao, J. R. A. Smit, G. Rijnders, M. Huijben, and G. Koster, *Appl. Phys. Lett.* **105**, 131906 (2014).